Order, miscibility, and electronic structure of $Ag(Bi,Sb)Te_2$ alloys and (Ag,Bi,Sb)Te precipitates in rocksalt matrix: A first-principles study

S. V. Barabash and V. Ozolins
Department of Materials Science and Engineering, University of California, Los Angeles, California 90095-1595, USA
(Received 5 October 2009; published 23 February 2010)

Using first-principles density-functional theory calculations and cluster expansion, we predict that $AgBiTe_2$-$AgSbTe_2$ alloys exhibit D4 cation order at all temperatures below melting and are fully miscible down to the room temperature and below. We also discuss the miscibility and ordering on the cation sublattice in quasiternary (Ag,Bi,Sb)Te alloys with general composition, within the subclass of structures with rocksalt topology (relevant for the case of coherent precipitates in a rocksalt matrix, e.g., in PbTe). The band structures of the $AgBiTe_2$ and $AgSbTe_2$ compounds and the evolution of the Fermi-surface topology at low hole dopings are presented. We use these results to refine the interpretation of the recent experimental measurements on naturally doped $AgSbTe_2$ samples reported by Jovovic and Heremans [Phys. Rev. B **77**, 245204 (2008)] and present a simplified model of the band dispersion near the valence-band maximum.

DOI: 10.1103/PhysRevB.81.075212 PACS number(s): 64.70.kg, 63.20.dk, 61.66.Fn, 64.75.Qr

I. INTRODUCTION

The ongoing search for better thermoelectrics has seen a number of recent experimental breakthroughs in materials based on bulk rocksalt tellurides: those include the high thermoelectric figure of merit ZT measured in $AgPb_mSbTe_{2+m}$ "LAST" alloys [$ZT \sim 2$ at $T=800$ K (Ref. 1)], high ZT measured in Tl-doped PbTe [$ZT \sim 1.5$ at $T=750$ K (Ref. 2)], and the demonstration of minimal thermal conductivity in $AgSbTe_2$.[3] Furthering such advances depends crucially on our knowledge of the structural properties and phase diagram behavior of telluride alloys—the subject that is not unambiguously established, despite decades of research. For instance, the record ZT values reported for $AgPb_mSbTe_{2+m}$ have been linked[1,4,5] to the development of nanoscale inhomogeneities, indicating that the average alloy composition exceeds the miscibility limits, as was recently confirmed by a theoretical first-principles examination establishing a wide miscibility gap.[6] This, however, overturned the last century's reports[7] of full miscibility in such alloys. Similarly, the recent results for ordering on the cation sublattice in $AgSbTe_2$ (Refs. 5, 6, and 8) overturned the previous reports of cation disorder in this compound.[9] As the search for better thermoelectrics extends to other alloys, the structure and miscibility limits in a wide range of thermoelectric alloys need to be reliably established, and the electronic band structure and its derivative properties characterized in detail.

A large body of the existing literature on bismuth-rich and antimony-rich tellurides is devoted to their nonrocksalt form, in particular, to the $(Bi,Sb)_2Te_{3-\delta}$ phase,[10] with some attention also given to the BiTe phase (with the BiSe structure[11]). Here, we focus on rocksalt-based structures, which become stabilized with the addition of silver, with both $AgSbTe_2$ and $AgBiTe_2$ stable at high temperatures.[9,12–14] At lower temperatures, the rocksalt $AgBiTe_2$ decomposes into[8,13,14] the nonrocksalt phases Ag_2Te and Bi_2Te_3, and $AgSbTe_2$ closely competes with[6,15,16] the $Ag_2Te+Sb_2Te_3$ mixture, yet metastable rocksalt compounds can be produced by rapid quenching. $AgBiTe_2$-$AgSbTe_2$ alloys[14] appear to exhibit full miscibility; however, recent challenges[1,4,6] to similar reports of full miscibility in the PbTe-$AgSbTe_2$ system and the reports of some segregation of $AgBiTe_2$ (Ref. 17) make it important to re-examine the miscibility in the $Ag(Bi,Sb)Te_2$ system. The cation sublattice was recently found[5,6,8] to possess D4 (or "AF-IIb") order in $AgSbTe_2$, thus challenging the original reports[9,14] of cation disorder in both $AgSbTe_2$ and $AgBiTe_2$, and no data are available concerning ordering at other compositions in $Ag(Bi,Sb)Te_2$ alloys. Finally, the stability of rocksalt (Ag,Bi,Sb)Te alloys with compositions away from the $Ag(Bi,Sb)Te_2$ isoplethal section has not been systematically studied.

Here, we use first-principles density-functional theory[18] (DFT) calculations coupled with cluster expansion (CE) (Ref. 19) and Monte Carlo (MC) studies to analyze the phase identity, miscibility, electronic band dispersion, and Fermi-surface structure in the (Bi,Ag,Sb)Te system. Prompted by the recent experimental advances,[1–4] we focus on the alloy systems with *rocksalt* topology, maintained either as true equilibrium structures or within precipitating phases due to coherent constraints from a rocksalt matrix such as PbTe. We find that $AgBi_xSb_{1-x}Te_2$ alloys are fully miscible down to the room temperature and generally, rocksalt $Ag_{1-x-y}Bi_xSb_yTe$ alloys are miscible if constrained to the rocksalt lattice. Both $AgSbTe_2$ and $AgBiTe_2$, as well as their alloys, exhibit D4 cation order at all temperatures below melting. The band structures of $AgSbTe_2$ and $AgBiTe_2$ share qualitative and even quantitative similarities but lead to different absorption edges for direct optical transitions. In the view of the recent experimental measurements of hole Fermi surfaces in $AgSbTe_2$,[20] we find that the Fermi topology is more complex than that assumed experimentally, yet our refinement of the experimental de Haas-van Alphen data yields an estimate of the Fermi energy very close to the value estimated in Ref. 20. Finally, as an alternative to the parabolic model, we offer a model capturing the qualitative features of the band dispersion near the valence-band maximum (VBM).

II. COMPUTATIONAL DETAILS

We analyzed the phase stability in (Ag,Bi,Sb)Te alloys using the first-principles CE approach.[19] For the alloys with

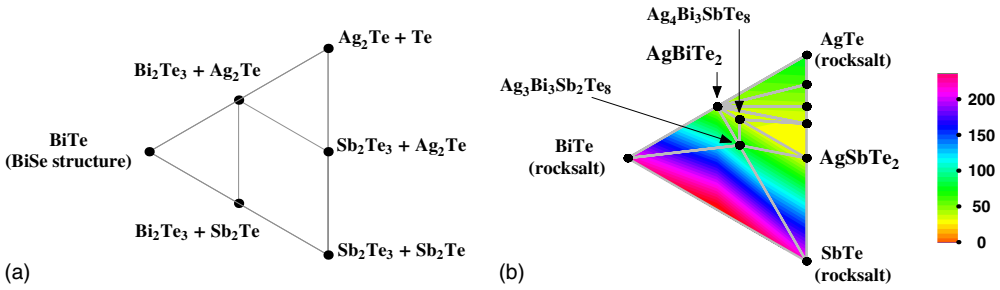

FIG. 1. (Color online) Gibbs triangle showing the $T=0$ stable structures along the $Ag_{1-x-y}Bi_xSb_yTe$ isoplethal section. Panel (a) shows the thermodynamically stable (nonrocksalt) structures and panel (b) shows the structures stable under a constraint of rocksalt topology. The color-coded background in the online version of panel (b) shows the $T=0$ energetic cost (in meV/cation) of forming a rocksalt system compared to the nonrocksalt structures of panel (a).

rocksaltlike topology, we started by calculating the DFT total energies E_{tot} of ordered $Ag_{1-x-y}Bi_xSb_yTe$ structures at zero pressure P. For each structure σ, the atoms were fully relaxed from the original ideal rocksalt positions.[21] We separately relaxed each structure within both the local-density approximation (LDA) (Ref. 22) and the generalized-gradient approximation (GGA) (Ref. 23) to the DFT, as we found some minor differences between the predictions of the two approximations (see Appendix). We used the projector-augmented wave method[24] as implemented in the VASP code.[25] The formation energy ΔH of structure σ is defined with respect to the energies of pure rocksalt tellurides as

$$\Delta H(\sigma) = E_{tot}(\sigma) - (1-x-y)E_{tot}(\mathrm{AgTe}) - xE_{tot}(\mathrm{BiTe}) - yE_{tot}(\mathrm{SbTe}),$$

where both E_{tot} and ΔH are given per cation site. The formation energies were numerically converged to $<\sim 1$ meV/cation.[26] The spin-orbit (SO) corrections were not included for ΔH calculations (see further discussion in the Appendix). The spin-orbit interactions were, however, included in our GGA calculations of the electronic band structure and the analysis of the Fermi-surface topology, described in Secs. IV and V.

The same numerical procedures were used for the calculations of the total energies of the experimentally known compounds with nonrocksalt lattice topologies: elemental Te in the γ-Se structure, Bi and Sb in the α-As structure, SbTe,[27] BiTe,[28] Sb_2Te,[29] Sb_2Te_3,[30] Bi_2Te_3,[31] and AgTe in the empressite[32] and sphalerite[33] structures (both observed only as metastable structures[34]), and Ag_2Te in the hessite[35] modification. The energies of these select structures were then used to assess the competition with the rocksalt alloys covered by our CE.

From the calculated LDA formation enthalpies ΔH^{LDA} of rocksalt-based structures, we constructed an effective Hamiltonian (LDA-CE) using a quasiternary CE formalism as implemented in the Alloy-Theoretic Automated Toolkit (ATAT).[36] The accuracy of the CE in predicting the energies of unknown structures was evaluated using the cross-validation score s_{CV} as implemented in ATAT.[36] The LDA-CE was iteratively improved by increasing the set of input structures $\{\sigma\}$. The final cluster expansion[37] is based on the energies of 175 structures and has the accuracy $s_{CV}^{\mathrm{LDA\text{-}CE}}=15$ meV/cation. We then calculated the GGA formation enthalpies ΔH^{GGA} for the same 175 structures and used them to construct a GGA-CE, with an accuracy of $s_{CV}^{\mathrm{GGA\text{-}CE}}=19$ meV/cation. The relatively large cross-validation error is largely related to the difficulty in predicting the energetics over a wide composition range by a single effective Hamiltonian. The two CE versions were independently used to identify the ground-state structures among all possible structures with up to 20 atoms in unit cell ($\sim 10^5$ structures) and to evaluate the phase stability at finite temperatures by means of Metropolis MC as implemented in ATAT.[36] The ordering temperatures were extracted from the $E(T)$ curves and the order type was determined by the analysis of the snapshots from simulated annealing MC runs. The miscibility was evaluated by scanning the Bi and Sb chemical potentials and performing a simulated annealing run for each combination of the chemical potentials, as explained in the Appendix.

III. PHASE STABILITY

In Fig. 1(a), we show the calculated $T=0$ K phase diagram of the $Ag_{1-x-y}Bi_xSb_yTe$ alloy system. We see that at low temperatures, the thermodynamically stable phases are all of *nonrocksalt* topology. With the exception of pure BiTe, each point in Fig. 1(a) corresponds to an equilibrium of two, three, or four phases because Fig. 1(a) shows the isoplethal section with 1:1 cation:anion ratio while this ratio is different in most of the $T=0$ K stable phases. Note that at $T=0$ K, the native (BiSe structure) form of SbTe has a higher energy than the two-phase mixture of Sb_2Te and Sb_2Te_3, suggesting that SbTe is only stabilized at higher temperatures by entropic effects.[11,38] Similarly, for a range of compositions, the rocksalt phases become thermodynamically stable at higher temperatures. Indeed, our numerical analysis of the vibrational contributions indicates that the rocksalt $AgSbTe_2$ and $AgBiTe_2$ become stabilized over the competing nonrocksalt phases at high temperatures, as we further discuss in the Appendix. We did not quantify the temperature-composition region where this stabilization occurs but focus on the rocksalt structures by merely assuming that a constraint of a rocksalt topology is applied,[39] e.g., due to coherent constraints inside a rocksalt matrix. Note that this topological constraint does not imply any restriction on *local* atomic relaxation away from perfect rocksalt positions nor does it require an application of an external strain.

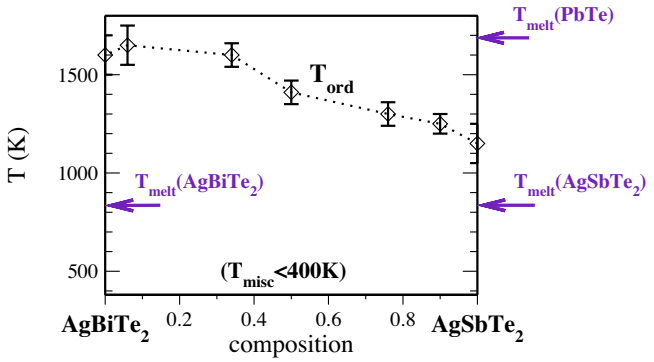

FIG. 2. (Color online) Calculated solid-state phase diagram of $AgBi_{1-x}Sb_xTe_2$ solid solutions, showing the order-disorder transition temperature T_{ord} of the D4 ordered phase and a schematic upper bound on the T_{misc} of the $AgBiTe_2$-$AgSbTe_2$ miscibility gap. Also marked are the experimental melting temperatures T_m of pure bulk $AgSbTe_2$, $AgBiTe_2$, as well as that of PbTe, which could serve as a coherent matrix for $Ag(Bi,Sb)Te_2$ precipitates.

Under such rocksalt constraints, several structures are stable at $T=0$. Figure 1(b) shows the GGA predictions for these structures (black points), as well as the $T=0$ energy differences (represented by the shading of the background) between such rocksalt-constrained alloys and the nonrocksalt ground-state structures of Fig. 1(a). One can see that for low Ag content, the energetic cost of forming rocksalt structures is prohibitive (up to ~200 meV/cation) and it is unlikely that alloys would adopt a rocksalt topology even under coherency constraints. On the other hand, around the $Ag(Bi,Sb)Te_2$ composition and for higher Ag content, the energy differences are lower and the entropy differences between the competing phases could stabilize the rocksalt phases at higher temperatures. We next focus on the $Ag(Bi,Sb)Te_2$ line in Fig. 1(b).

Both for $AgSbTe_2$ and $AgBiTe_2$, we predict D4 cation ordering of cubic symmetry.[40,41] In Fig. 2, we show the calculated solid-state temperature-composition phase diagram for the $Ag(Bi,Sb)Te_2$ isoplethal section. The rocksalt $Ag(Bi,Sb)Te_2$ alloys maintain the D4-type ordering of Ag vs (Bi,Sb) cations at all compositions. Further, the D4 ordering temperature T_{ord}, predicted by LDA-CE MC in the assumption that the alloys remain solid (the dotted line in Fig. 2), substantially exceeds the experimental melting temperatures T_m of pure bulk $AgSbTe_2$ and $AgBiTe_2$ (shown by the arrows). Thus, the alloys maintain D4 order at all temperatures below the melting temperature. One can see that $AgSbTe_2$ and $AgBiTe_2$ are fully miscible at all experimentally relevant temperatures, as we explicitly confirmed with MC down to at least 400K. The energetic competition at very low temperatures could not be uniquely established, as it turns out to be different in the predictions of LDA and GGA. For example, an ordered structure at $Ag_4Bi_3SbTe_8$ composition has a lower energy than the $AgSbTe_2$+$AgBiTe_2$ mixture in the GGA, as reflected in Fig. 1(b) but not in the LDA (see the Appendix for further details). At the experimentally relevant temperatures, the corresponding energy differences (~10 meV/cation) are much smaller than the entropic contributions to the free energy of a disordered (Bi,Sb) sublattice; indeed, down to 400 K, no ordering within the (Bi,Sb) sublattice was found in simulated annealing runs based on both GGA-CE and LDA-CE.

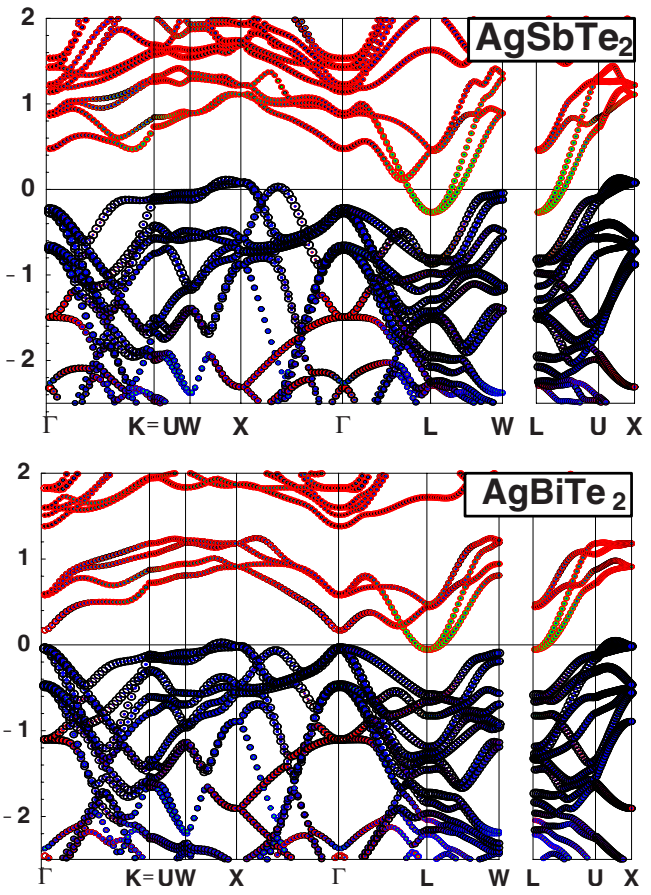

FIG. 3. (Color online) Band structure of ordered $AgSbTe_2$ and $AgBiTe_2$. The radii of the color circles in the online version are proportional to the contributions from Te 5*p* (black), Ag 4*d* (blue), Ag 5*s* (green), and Bi 6*p* or Sb 5*p* (red). The energies are relative to the calculated value of the Fermi level.

The full miscibility at $T>400$ K applies not only along the $Ag(Bi,Sb)Te_2$ isoplethal section but appears to extend to all compositions under the rocksalt constraint (see further details of the miscibility analysis in the Appendix). The only limitation on the experimentally obtainable compositions of (Ag,Bi,Sb)Te rocksalt alloys comes from their direct competition with nonrocksalt phases. We thus speculate that a wide range of compositions could be obtained for coherently precipitating phases immiscible with a suitable rocksalt matrix, such as PbTe.

IV. BAND STRUCTURE

Figure 3 shows the band structures of $AgSbTe_2$ and $AgBiTe_2$, both with the D4 ("AFM-IIb") cation ordering predicted by our cluster expansion and confirmed by DFT. The circles of varying radii denote the contributions from different atomic orbitals, as detailed in the figure caption. The $AgSbTe_2$ band structure previously calculated by Hoang *et al.*[8] and Ye *et al.*[41] agrees well with our results. We now

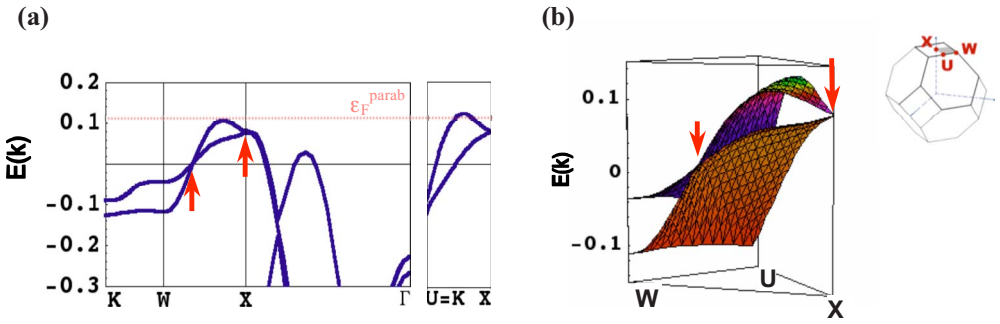

FIG. 4. (Color online) Dispersion of $AgSbTe_2$ valence bands, (a) for select directions and (b) within W-X-U facet of the Brillouin zone (shown in the inset). The dashed line in (a) corresponds to the measured Fermi level ε_F^{parab} (Ref. 20). The arrows highlight the band crossing points with conical energy dispersion. Band energies are relative to the GGA value of Fermi level ε_F^{GGA}.

compare it with the $AgBiTe_2$ band structure and in the next section compare the DFT predictions with the recent experimental determination of the $AgSbTe_2$ Fermi surface.[20]

Both in $AgSbTe_2$ and $AgBiTe_2$, the primary sources of holes are the states near the X point in the two valence bands of predominantly Te $5p$ character. The considerable hybridization of these bands with the Ag $4d$ states (blue circles in the online version) may be somewhat overestimated by the GGA, as suggested by an earlier "screened-exchange" (LDA) investigation.[41] The VBM is near the X point on the X-U line and the dispersion of the top valence band is quite flat along the X-W, W-K(=U), and X-U directions. The conduction bands are predominantly of Sb $5p$ (in $AgSbTe_2$)/Bi $6p$ (in $AgBiTe_2$) character, with the conduction-band minimum (CBM) located at the L point in both materials.

The relative position of the CBM and VBM, and the actual position of the Fermi level cannot be reliably established within the semilocal forms of the exchange-correlation potential such as the GGA due to the well-known band-gap problem. Within the GGA, the valence and conduction bands overlap substantially, leading to a Fermi level ε_F^{GGA} positioned 122 meV (38 meV) below the VBM in $AgSbTe_2$ ($AgBiTe_2$) and to a presence of both holelike and electronlike Fermi surfaces. Band-gap corrections reduce[41] the predicted overlap, likely opening a small band gap. In this case, the position of the Fermi level and the shape of the Fermi surfaces (if any) would strongly depend on the presence and identity of defects, reflecting the experimental conditions during sample preparation.

As discussed in the Appendix, the difference between the $AgSbTe_2$ and $AgBiTe_2$ band structures is largely due to the spin-orbit effects. The main difference in the band dispersions is near the Γ point: in $AgSbTe_2$, the valence-band energy at the Γ point is considerably (0.35 eV) below the VBM, whereas in $AgBiTe_2$, it is only 76 meV below the VBM. Similarly, the conduction band at Γ is much closer to the CBM in the case of $AgBiTe_2$ (although still 0.24 eV above the CBM). This changes the absorption edge for direct transitions: in $AgSbTe_2$, it is shaped by the contributions from a large part of the L-U-W facet of the Brillouin zone (where the direct gap is nearly constant), whereas in $AgBiTe_2$, the direct gap at Γ clearly defines the absorption edge. Another interesting feature of the $AgBiTe_2$ band structure, not present in $AgSbTe_2$, is a considerable separation between two sets of conduction bands due to spin-orbit coupling effects, which leads to a second "gap" ~1.3 eV above the Fermi level (the existence and the size of this gap could be affected by the band alignment corrections and thus are not investigated in detail here).

V. DISPERSION NEAR VBM AND $AgSbTe_2$ FERMI SURFACE

For $AgSbTe_2$, Jovovic and Heremans[20] have experimentally established that the samples of pure material obtained by conventional solid-state chemistry correspond to a naturally hole-doped narrow-gap semiconductor with an indirect gap of less than 10 meV. Within the parabolic band approximation, they estimated that the Fermi level crosses valence bands at $\varepsilon_F^{parab}(T=0\ \mathrm{K})=\varepsilon_{\mathrm{VBM}}-15$ meV. Based on the Fermi-surface topology predicted by the GGA in Ref. 42, they further assumed that the majority carriers come from two concentric Fermi pockets around each X point. Approximating the GGA-predicted dispersion of the two hole bands by a parabolic model, they found that the maximal areas of the Fermi cross sections corresponding to this experimental ε_F^{parab} agreed well with the areas inferred from their de Haas-van Alphen measurements, thus independently reconfirming the ε_F^{parab} value.

We caution here that while the GGA does predict two concentric Fermi pockets around X *at the GGA value* of the Fermi level ε_F^{GGA}, it rules out such a topology for the measured value ε_F^{parab}. Indeed, as seen in Fig. 4(a), the actual VBM is determined by only one of the two valence bands, which peaks somewhat away from the X point at the S (X-U) line. The second band peaks at the X point where the two bands become degenerate. The Fermi level at ε_F^{parab} (the dashed line) only crosses one of the two valence bands, leading to a single Fermi surface around X. In what follows, we examine the GGA-calculated Fermi surface and reanalyze the de Haas-van Alphen results of Ref. 20.

Before analyzing the topology of the Fermi surface, we note a few features of the band structure that are clearly visible from Figs. 4(a) and 4(b). The two valence bands exhibit an avoided crossing behavior, becoming degenerate at isolated lines in the three-dimensional Brillouin zone. These lines intersect the X-U-W facets at the X point and at one

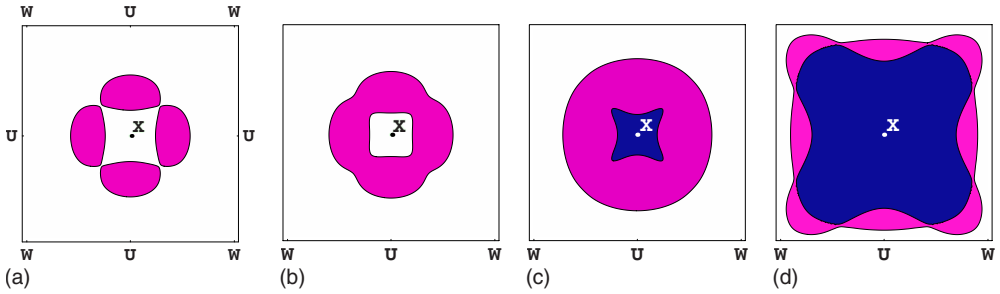

FIG. 5. (Color online) The (100) cross sections of the Fermi pockets for different positions of ε_F relative to the VBM: (a) $\varepsilon_{\mathrm{VBM}}-\varepsilon_F=15$ meV, (b) 20 meV, (c) 60 meV, and (d) 160meV. The full X-centered facet of the Brillouin-zone boundary is shown as labeled in (a). In (c) and (d), the larger (light pink) Fermi pocket also fills the space occupied by the smaller (dark blue) pocket.

more point on each Z (X-W line), with a characteristic conical dispersion in the vicinity of each crossing point (highlighted by the arrows in Fig. 4). The lower band has a maximum at X point, at the energy $\varepsilon_X=\varepsilon_{\mathrm{VBM}}-43$ meV in the case of $AgSbTe_2$ (or at $\varepsilon_X=\varepsilon_{\mathrm{VBM}}-55$ meV in $AgBiTe_2$). However, the electronic density of states does not show a visible feature at this band maximum since the conical dispersion within the X-U-W plane leads to a very weak van Hove singularity ($\sim|\varepsilon-\varepsilon_X|^{3/2}$ instead of the usual $\sim|\varepsilon-\varepsilon_X|^{1/2}$).

The evolution of the topology of the Fermi surface with ε_F is illustrated in Fig. 5. For ε_F near $\varepsilon_{\mathrm{VBM}}$, the upper valence band forms a multiply connected Fermi surface. As ε_F is gradually lowered (hole concentration increased), the four small disjoint Fermi pockets clustered around each X point [shown in Fig. 5(a)] merge to form a single ring-shaped pocket seen in Fig. 5(b). Upon further decrease in ε_F, the Fermi level moves into the second valence band and a new Fermi sheet appears, as the large ring-shaped pocket of Fig. 5(b) changes its topology again to become singly connected, see Figs. 5(c) and 5(d). This results in the two concentric Fermi surfaces as assumed in Ref. 20 but requires at least a threefold increase in $\varepsilon_F-\varepsilon_{\mathrm{VBM}}$ compared to the experimental estimate ε_F^{parab}. For very large dopings (in $AgSbTe_2$, for $\varepsilon_F<\varepsilon_{\mathrm{VBM}}-93$ meV), an additional Fermi sheet (not shown in Fig. 5) develops along the X-Γ line. The experimental hole concentration corresponds roughly to the crossover between the Fermi topologies of Figs. 5(a) and 5(b).

We can now give a specific estimate of ε_F corresponding to the experimental de Haas-van Alphen measurements of Ref. 20 by calculating the GGA-predicted areas of the Fermi cross sections. The two broad peaks in the experimental data give the extremal areas of Landau orbits normal to the ⟨111⟩ direction. In Fig. 6, we show the dependence of the GGA-predicted extremal areas A_F^{ext} for a series of presumed ε_F values. The bold symbols indicate the features expected to give major contribution to the de Haas-van Alphen oscillations (see the Appendix for further discussion). The gray lines in Fig. 6 indicate the positions of the experimental peaks. A reasonable agreement is achieved if the Fermi level is presumed to lie within $\varepsilon_F^{dHvA}=\varepsilon_{\mathrm{VBM}}-17\cdots19$ meV range, not far from the experimental estimate $\varepsilon_F^{parab}=\varepsilon_{\mathrm{VBM}}-15$ meV.

We obtained the above estimates using a detailed fit to the calculated band structure of $AgSbTe_2$. We also offer a simpler semiquantitative model of the valence-band dispersion near the VBM, as an improvement to the overly simplified parabolic model. For a $\mathbf{k}$ in the vicinity of a Fermi pocket [e.g., of the ring in Fig. 5(b)], we approximate the energy in terms of the cylindrical components of $\mathbf{k}=k_\perp\hat{z}+k_R\cos 2\phi\hat{x}+k_R\sin 2\phi\hat{y}$ as parabolic in $k_\perp$ and k_R with the maxima at $k_\perp=0$ and $k_R=k_{\max}$, respectively, and choose the simplest form of the angular dependence that has a clear mapping to its parabolic approximant,

$$\varepsilon(\mathbf{k})\approx\varepsilon_0-\frac{\hbar^2k_\perp^2}{2m_\perp}-\frac{\hbar^2(k_R-k_{\max})^2}{2m_R}-\frac{\hbar^2(k_{\max}/4)^2}{m_\phi}\cos 4\phi, \tag{1}$$

here $m_\perp\approx(1.22\pm0.10)m_e$, $m_R\approx(3.0\pm0.7)m_e$, $m_\phi\approx(3.1\pm0.2)m_e$, $k_{\max}\approx(0.137\pm0.004)\pi/a$, m_e is the free-electron mass, and a is the lattice constant of the D4 structure (1.21 nm in experiment and 1.24 nm in GGA). The uncertainty in the fit parameters is due to both the higher-order contributions and the variation in $m_\perp$, m_R, and $k_{\max}$ with ϕ. This model becomes inaccurate far from VBM ($\varepsilon\ll\varepsilon_{\mathrm{VBM}}-40$ meV) and explicitly breaks down as $k_R\to0$ but it gives a reasonable approximation to the energies near the VBM and around the estimated Fermi level (ε_F^{dHvA} or ε_F^{parab}).

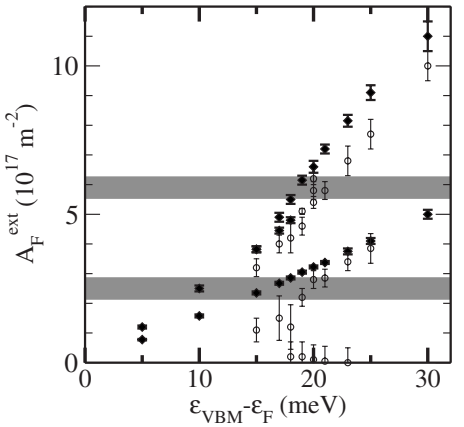

FIG. 6. The extremal values of the Fermi cross-section area A_F vs the presumed position of the Fermi level ε_F. The bold symbols indicate the features giving the largest contribution to the de Haas-van Alphen signal (see Appendix). The wide horizontal gray lines correspond to the de Haas-van Alphen measurements of Ref. 20.

In particular, Eq. (1) gives the correct energy difference between the VBM (at the X-U line) and the saddle point at the X-W line, $2\frac{\hbar^2(k_{\max}/4)^2}{m_\phi} \approx 15$ meV. Since our model captures the qualitative changes in the Fermi topology, it could be used instead of the conventional parabolic model for hole carriers in $AgSbTe_2$.

Surprisingly, Eq. (1) also yields a good model for the dispersion near the VBM in $AgBiTe_2$. Indeed, the differences in $m_\perp$, m_R, m_ϕ, and $k_{\max}$ fitted for $AgSbTe_2$ and $AgBiTe_2$ are smaller than the uncertainties cited above.

VI. CONCLUSIONS

We have found that $AgBi_xSb_{1-x}Te_2$ alloys exhibit D4 ordering of Ag vs (Bi,Sb) cations and are fully miscible down to the room temperature. Generally, $Ag_{1-x-y}Bi_xSb_yTe_2$ alloys are miscible if constrained to the rocksalt lattice. Without such a constraint, nonrocksalt phases become thermodynamically stable at all compositions at sufficiently low temperatures. The band structures of $AgSbTe_2$ and $AgBiTe_2$ share many similarities; in particular, in both compounds the dispersion around the VBM is reasonably approximated by Eq. (1). However, stronger spin-orbit coupling in Bi-containing materials changes some band-structure features by up to ~ 1 eV, in particular, leading to a different absorption edge for direct optical transitions and a second gap at $\sim \varepsilon_F + 1.3$ eV seen in $AgBiTe_2$ dispersion. The topology of the Fermi surface is sensitive to the hole doping. A detailed analysis of the experimental de Haas-van Alphen data based on the calculated band structure suggests the Fermi level in naturally doped samples is located around $\varepsilon_F^{dHvA} = \varepsilon_{\mathrm{VBM}} - 17 \cdots 19$ meV, not far from the value estimated in Ref. 20.

ACKNOWLEDGMENTS

This work has been supported the U.S. Department of Energy EFRC on "Revolutionary Materials for Solid State Energy Conversion." The calculations in this research were supported by NSF through TeraGrid resources provided by SDSC, NCSA, and TACC.

APPENDIX

1. Spin-orbit effects

The SO coupling strongly affects the band structures of the alloys studied here. For example, the direct gap at Γ point is small in $AgBiTe_2$ but not in $AgSbTe_2$ (cf. Fig. 3) and this difference is due to the SO coupling. Another example is the gap between the two sets of the $AgBiTe_2$ valence bands, which disappears if the SO interaction is neglected (in fact, scalar-relativistic calculations for $AgBiTe_2$ lead to a band structure quite similar to that of $AgSbTe_2$). At the same time, the effect of the SO corrections on the formation energies (ΔH's) is small for (Ag,Sb)Te alloys (cf. the supplementary material in Ref. 6) due to averaging over contributions from different parts of the Brillouin zone. However, even the ΔH values are affected in Bi-containing alloys, as seen from Table I. Still, the SO corrections do not appear to change the energetic hierarchy and their effect on ΔH's is comparable to the difference between the scalar-relativistic LDA and GGA results. Thus, to reduce the computational cost, we only used the scalar-relativistic LDA and GGA for the ΔH calculations.

TABLE I. Comparison of the formation energies of select $AgSbTe_2$ and $AgBiTe_2$ structures calculated in the GGA with spin-orbit coupling (GGA+SO), and in the scalar-relativistic GGA and LDA.

		ΔH (meV/cation)		
Composition	Cation ordering	GGA+SO	GGA	LDA
$AgSbTe_2$	D4	−183.6	−189.1	−149.6
	$L1_1$	−174.2	−187.2	−147.9
	$L1_0$	−85.9	−75.0	−29.8
$AgBiTe_2$	D4	−129.5	−213.4	−176.4
	$L1_1$	−129.1	−212.3	−173.8
	$L1_0$	+17.9	−28.1	+45.4

2. Monte Carlo analysis of miscibility

We evaluated the miscibility in rocksalt-constrained (Ag,Sb,Bi)Te alloys by scanning the chemical potentials $\{\mu_{\mathrm{Sb}}, \mu_{\mathrm{Bi}}, \mu_{\mathrm{Ag}}\}$ with a step of 10 meV in $\mu_{\mathrm{Sb}} - \mu_{\mathrm{Ag}}$ and $\mu_{\mathrm{Bi}} - \mu_{\mathrm{Ag}}$, and for each combination performing a semigrand-canonical simulated annealing run using ATAT Monte Carlo routines.[36] In Fig. 7, we illustrate how the resulting equilibrium compositions evolve from 800 to 400 K. Each point in Fig. 7 indicates a composition inside a Gibbs triangle, achieved at some given $\{\mu_{\mathrm{Sb}}, \mu_{\mathrm{Bi}}, \mu_{\mathrm{Ag}}\}$ combination; the regions between the points may either correspond to intermediate chemical-potential values or indicate an opening of a miscibility gap. We see that the attainable compositions span throughout the Gibbs triangle, without major miscibility gaps down to 400 K. The densely grouped regions along the $AgSbTe_2$-$AgBiTe_2$ line reflect the small composition changes upon varying μ_{Ag}, whereas the several narrow gaps along that line reflect larger composition changes upon varying $\mu_{\mathrm{Sb}} - \mu_{\mathrm{Bi}}$. In Ag-poor, Bi-rich alloys, a narrow gap may be opening below ~500 K; we did not investigate this in

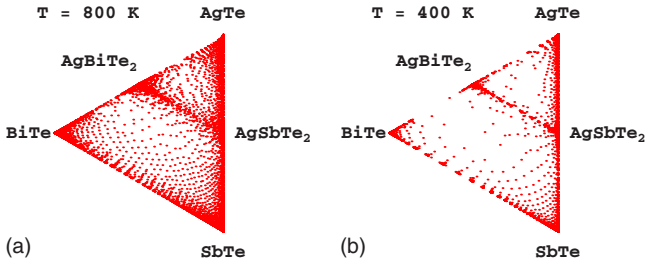

FIG. 7. (Color online) Evolution of equilibrium compositions of rocksalt-constrained (Ag,Bi,Sb)Te alloys from 800 to 400 K for a finite set of chemical-potential combinations $\{\mu_{\mathrm{Sb}}, \mu_{\mathrm{Bi}}, \mu_{\mathrm{Ag}}\}$. Each point indicates a composition achieved at some $\{\mu_{\mathrm{Sb}}, \mu_{\mathrm{Bi}}, \mu_{\mathrm{Ag}}\}$; the regions between the points correspond either to intermediate chemical-potential values or to immiscible compositions.

TABLE II. The formation energies of the ground-state predictions (typeset in regular font) and of some of the competing low-energy structures (typeset in italic and parenthesized) along $AgSbTe_2$-$AgBiTe_2$ isoplethal section as given by direct DFT calculations or by CE using both the LDA and the GGA.

		ΔH (meV/cation)			
Composition	Cation ordering	LDA	LDA-CE	GGA	GGA-CE
$AgSbTe_2$	D4	−149.8	−142.0	−177.9	−166.0
	$L1_1$	*(−147.9)*	−142.0	*(−172.8)*	*(−164.8)*
$AgBiTe_2$	D4	−176.4	−170.1	−213.4	−204.2
	$L1_1$	*(−173.8)*	*(−164.8)*	*(−212.3)*	*(−191.0)*
$Ag_4Bi_3SbTe_8$	$L1_1$-based (16 atoms)	*(−164.6)*	*(−155.1)*	−206.6	*(−187.9)*
	D4-based (256 atoms)		*(−158.5)*		*(−193.2)*
	Two-phase mixture ($AgSbTe_2$+$AgBiTe_2$)	−169.8	−163.1	*(−204.5)*	−194.7

detail since at these compositions, the energetic cost of imposing the rocksalt restriction is prohibitive at low T [$\sim$0.3 eV/atom at T=0, cf. Fig. 1(b)].

3. Vibrational stabilization of rocksalt structures

The vibrational frequencies were evaluated for the native forms of Ag_2Te, Sb_2Te_3, and Bi_2Te_3, and for the rocksalt-based D4-ordered $AgSbTe_2$ and $AgBiTe_2$, using the dynamical matrix calculated for a supercell with 128 ($AgSbTe_2$, $AgBiTe_2$) 144 (Ag_2Te) or 135 (Sb_2Te_3, Bi_2Te_3) atoms. The vibrational contributions to the free energy were then evaluated within the harmonic approximation. The details of the method are given in Ref. 43. For $AgSbTe_2$, we find that it is stabilized with respect to Ag_2Te+Sb_2Te_3 at T $\sim$500 K (within the LDA). Since the differences in both the vibrational and the cohesive contributions to the free energy of the competing phases are very small, this should be treated as a very crude estimate. For $AgBiTe_2$, we find indications of slight phonon instabilities, which invalidate the standard harmonic entropy formalism. Nevertheless, the instabilities are very small: even within the GGA (in which the instabilities are most prominent), the mode with the largest imaginary frequency leads to the energy lowering of no more than 1 meV/atom. Thus, the phonon-phonon coupling would likely stabilize this mode at higher temperatures, due to anharmonic stabilization effects seen, for example, in bcc Zr.[44] Under reasonable assumptions for the renormalized values of the vibrational frequencies at higher temperatures, $AgBiTe_2$ is also stabilized with respect to Ag_2Te+Bi_2Te_3 at a few hundred degrees Celsius.

4. Ground state predictions in LDA vs GGA

In Table II, we show the formation energies of select ordered structures[40] along the $AgSbTe_2$-$AgBiTe_2$ isoplethal section as calculated directly with DFT and as fitted (or predicted) by CE using both the LDA and the GGA. For each energy functional, the table lists the ground-state predictions (typeset in regular font), as well as some of the competing low-energy structures that are *not* ground states (typeset in italic and parenthesized). We see that the lowest energy structures exhibit Ag vs (Bi,Sb) ordering based on one of the two closely related[6,45] binary structures, D4 and $L1_1$. For the ternary compounds ($AgSbTe_2$ and $AgBiTe_2$), D4 ordering yields a slightly lower energy than $L1_1$. At quaternary compositions and within the GGA, the search limited to structures with $<$20 atoms/cell identified a 16-atom $L1_1$-based $Ag_4Bi_3SbTe_8$ ground-state structure that in direct GGA calculations indeed had a lower energy than the $AgSbTe_2$ +$AgBiTe_2$ mixture. Within the LDA, this structure is unstable with respect to D4 $AgSbTe_2$+D4 $AgBiTe_2$. From the latter fact, we conclude that such fine details of energetic competition along $AgSbTe_2$-$AgBiTe_2$ line cannot be resolved within the accuracy of the LDA and/or GGA. Note that at the same $Ag_4Bi_3SbTe_8$ composition, the simulated annealing results based on both GGA-CE and LDA-CE indicate that a 256-atom D4-based structure (which we deemed too large to be tested directly in DFT) could have an even lower energy than this directly calculated 16-atom $L1_1$-based structure, consistent with the D4 order observed at higher temperatures.

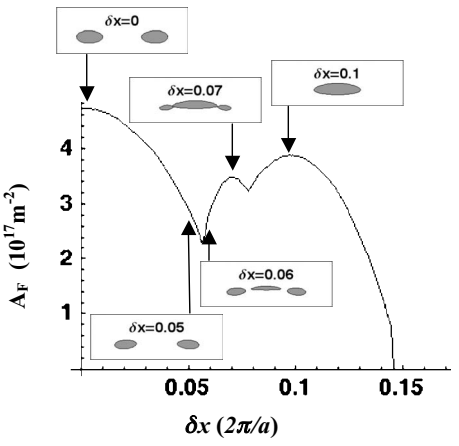

FIG. 8. The area A_F of the Fermi-surface ⟨111⟩ cross section vs the position δx of the cross-sectioning plane, relative to the X point. The insets show the shape of the cross section(s) for a few values of δx. In cases of multiple cross sections seen in the insets, the main figure shows the net area of all cross sections in the vicinity of a given X point.

5. de Haas-van Alphen analysis

To identify the GGA extremal areas, we first assume a value of ε_F and then vary the position δx of a $\langle 111 \rangle$ plane $\wp$ (in $\boldsymbol{k}$ space) to numerically calculate the net area A_F of the Fermi orbit(s), i.e., the area occupied by points $\boldsymbol{k}$ in the plane $\wp$ satisfying $\varepsilon(\mathbf{k}) > \varepsilon_F$. (Technically, only the portion of $\wp$ in the general vicinity of a single X point is considered.) We performed the integration of the GGA band structure in dimensionless units of $ka/2\pi$ and then used the experimental value of the lattice parameter a to determine A_F. In Fig. 8 we show an example of how A_F depends on the position δx of the cross-sectioning $\langle 111 \rangle$ plane. The insets show the shape of the cross sections for a few select values of δx. We see three broad maxima at $\delta x = 0$ (corresponding to the net area of the two "necks" of the ring-shaped Fermi surface, maximized by a $\langle 111 \rangle$ plane passing through an X point) and at $\delta x \approx 0.07$ and $\delta x \approx 0.1$ (corresponding to the maximal areas of a single cross section). The Landau orbits corresponding to these maxima give the leading contributions to the Frenel-type integrals of the electronic energy and should lead to well-defined de Haas-van Alphen oscillations. In Fig. 6, we show these areas by bold symbols. A number of additional extremal features can be inferred from Fig. 8, corresponding to topological changes in $A_F(\delta x)$ (e.g., a single orbit being split into two or three smaller orbits) or otherwise reflecting the complexity of the Fermi surface (e.g., a sharp minimum at $\delta x \approx 0.08$). While such features may be important in the $T \to 0$ limit, the thermal broadening would likely mask them against the background contribution from all other parts of the Fermi surface. We show the areas corresponding to these features by thin symbols in Fig. 6.

[1] K. F. Hsu, S. Loo, F. Guo, W. Chen, J. S. Dyck, C. Uher, T. Hogan, E. K. Polychroniadis, and M. G. Kanatzidis, Science **303**, 818 (2004).

[2] J. P. Heremans, V. Jovovic, E. S. Toberer, A. Saramat, K. Kurosaki, A. Charoenphakdee, S. Yamanaka, and G. J. Snyder, Science **321**, 554 (2008).

[3] D. T. Morelli, V. Jovovic, and J. P. Heremans, Phys. Rev. Lett. **101**, 035901 (2008).

[4] Nancy Chen, Franck Gascoin, G. Jeffrey Snyder, Eckhard Müller, Gabriele Karpinski, and Christian Stiewe, Appl. Phys. Lett. **87**, 171903 (2005); H. Lin, E. S. Bozin, S. J. L. Billinge, E. Quarez, and M. G. Kanatzidis, Phys. Rev. B **72**, 174113 (2005); B. A. Cook, M. J. Kramer, J. L. Harringa, M.-K. Han, D.-Y. Chung, and M. G. Kanatzidis, Adv. Funct. Mater. **19**, 1254 (2009).

[5] E. Quarez, K. F. Hsu, R. Pcionek, N. Frangis, E. K. Polychroniadis, and M. G. Kanatzidis, J. Am. Chem. Soc. **127**, 9177 (2005).

[6] S. V. Barabash, V. Ozolins, and C. Wolverton, Phys. Rev. Lett. **101**, 155704 (2008).

[7] H. Fleischmann, Z. Naturforsch. A **16a**, 765 (1961) (in German); L. Borisova and S. Dimitrova, Phys. Status Solidi A **53**, 403 (1979); L. Borisova, Phys. Status Solidi B **126**, K155 (1984).

[8] K. Hoang, S. D. Mahanti, J. R. Salvador, and M. G. Kanatzidis, Phys. Rev. Lett. **99**, 156403 (2007).

[9] S. Geller and J. H. Wernick, Acta Crystallogr. **12**, 46 (1959).

[10] H. Scherrer and S. Scherrer, in *CRC Handbook of Thermoelectrics*, edited by D. M. Rowe (CRC, Cleveland, 1995), p. 211; M. Stordeur, *CRC Handbook of Thermoelectrics*, edited by D. M. Rowe (CRC, Cleveland, 1995), p. 239; R. Venkatasubramanian, E. Siivola, T. Colpitts, and B. O'Quinn, Nature (London) **413**, 597 (2001).

[11] N. K. Abrikosov and L. V. Poretskaya, Inorg. Mater. **1**, 462 (1965); G. Ghosh, J. Phase Equilib. **15**, 349 (1994).

[12] R. Schmid-Fetzer, Ternary Alloys, ASM Alloy Phase Diagrams Center, http://www.asminternational.org/AsmEnterprise/APD, ASM International, Materials Park, OH, 1988, Vol. 2, pp. 552–555.

[13] R. Schmid-Fetzer, Ternary Alloys, ASM Alloy Phase Diagrams Center, http://www.asminternational.org/AsmEnterprise/APD, ASM International, Materials Park, OH, 1988, Vol. 1, pp. 325–328; A. Stegherr, P. Eckerlin, and F. Wald, Z. Metallkd. **54**, 598 (1963) (in German).

[14] J. H. Wernick, S. Geller, and K. E. Benson, J. Phys. Chem. Solids **7**, 240 (1958).

[15] R. G. Maier, Z. Metallkd. **54**, 311 (1963) (in German).

[16] J. P. McHugh, W. A. Tiller, S. E. Haszko, and J. H. Wernick, J. Appl. Phys. **32**, 1785 (1961).

[17] T. Ono, T. Takahama, and T. Irie, J. Phys. Soc. Jpn. **17**, 1070 (1962).

[18] P. Hohenberg and W. Kohn, Phys. Rev. **136**, B864 (1964); W. Kohn and L. J. Sham, *ibid.* **140**, A1133 (1965).

[19] J. M. Sanchez, F. Ducastelle, and D. Dratias, Physica A **128**, 334 (1984).

[20] V. Jovovic and J. P. Heremans, Phys. Rev. B **77**, 245204 (2008).

[21] Here, the structure is defined as a particular decoration of a the cation sublattice by Ag, Bi, and Sb atoms, with the anion sites fully occupied by Te ions. We thus limit our study to the alloy systems with equal number of cation (Ag,Bi,Sb) and anion (Te) atoms, and neglect the presence of interstitials, vacancies, and cation-anion antisites.

[22] D. M. Ceperley and B. J. Alder, Phys. Rev. Lett. **45**, 566 (1980); J. P. Perdew and A. Zunger, Phys. Rev. B **23**, 5048 (1981).

[23] J. P. Perdew and Y. Wang, J. Chem. Phys. **45**, 13244 (1992).

[24] P. E. Blöchl, Phys. Rev. B **50**, 17953 (1994); G. Kresse and D. Joubert, *ibid.* **59**, 1758 (1999).

[25] G. Kresse and J. Hafner, Phys. Rev. B **48**, 13115 (1993); G. Kresse and J. Furthmüller, Comput. Mater. Sci. **6**, 15 (1996); Phys. Rev. B **54**, 11169 (1996).

[26] We used a basis set energy cutoff of 350 eV and dense k meshes corresponding to at least $16\,000/N_{\text{atoms}}$ k points in the first Brillouin zone, where N_{atoms} is the number of atoms in the supercell.

[27] M. M. Stasova, J. Struct. Chem. **8**, 584 (1967).

[28] H. Shimazaki and T. Ozawa, Am. Mineral. **63**, 1162 (1978).

[29] V. Agafonov, N. Rodier, R. Ceolin, R. Bellissent, C. Bergman, and J. P. Gaspard, Acta Crystallogr., Sect. C: Cryst. Struct. Commun. **47**, 1141 (1991).

[30] T. L. Anderson and H. B. Krause, Acta Crystallogr., Sect. B: Struct. Crystallogr. Cryst. Chem. **30**, 1307 (1974).

[31] Y. Feutelais, B. Legendre, N. Rodier, and V. Agafonov, Mater. Res. Bull. **28**, 591 (1993).

[32] L. Bindi, P. G. Spry, and C. Cipriani, Am. Mineral. **89**, 1043 (2004).

[33] I. R. Nuriev, R. M. Imamov, R. B. Shafizade, Sov. Phys. Crystallogr. **16**, 895 (1972).

[34] B. Predel, in *Phase Equilibria, Crystallographic and Thermodynamic Data of Binary Alloys*, edited by O. Madelung, Landolt-Börnstein, New Series, Group IV, Vol. 5a (Springer, Berlin, 1991), p. 212.

[35] A. van der Lee and J. L. de Boer, Acta Crystallogr., Sect. C: Cryst. Struct. Commun. **49**, 1444 (1993).

[36] A. van de Walle and G. Ceder, J. Phase Equilib. **23**, 348, (2002; A. van de Walle and M. Asta, Modell. Simul. Mater. Sci. Eng. **10**, 521 (2002); A. van de Walle, M. Asta, and G. Ceder, CALPHAD: Comput. Coupling Phase Diagrams Thermochem. **26**, 539 (2002).

[37] Our final GGA-CE includes 9 pair, 22 three-body, and 5 four-body coefficients; the LDA-CE includes 8 pair, 10 three-body, and 4 four-body coefficients.

[38] Experimentally, SbTe substantially deviates from the formal stoichiometry (Ref. 11), indicating that entropy may indeed yield decisive contributions to its stability at finite temperatures. Note that BiTe is stable even without a similar entropic stabilization: BiTe has a lower energy than the Bi_2Te and Bi_2Te_3 mixture in LDA, and is degenerate with this mixture in GGA.

[39] We refer to this topological constraint as "the rocksalt constraint," which does not imply fixing atoms to the ideal rocksalt positions.

[40] For cation ordering, we use the standard notatio for fcc alloy structures; for explicit definitions, see, e.g., S. V. Barabash, V. Ozolins, and C. Wolverton, Phys. Rev. B **78**, 214109 (2008).

[41] L.-H. Ye, K. Hoang, A. J. Freeman, S. D. Mahanti, J. He, T. M. Tritt, and M. G. Kanatzidis, Phys. Rev. B **77**, 245203 (2008).

[42] K. Hoang, Ph.D. thesis, Michigan State University, 2007.

[43] C. Wolverton, V. Ozolins, and M. Asta, Phys. Rev. B **69**, 144109 (2004).

[44] Y.-Y. Ye, Y. Chen, K.-M. Ho, B. N. Harmon, and P. A. Lindgard, Phys. Rev. Lett. **58**, 1769 (1987).

[45] A. Finel, Ph.D. thesis, University of Paris, 1987; Z. W. Lu, S. H. Wei, A. Zunger, S. Frota-Pessoa, and L. G. Ferreira, Phys. Rev. B **44**, 512 (1991); C. Wolverton and A. Zunger, J. Electrochem. Soc. **145**, 2424 (1998).